Commun. Comput. Phys.
doi: 10.4208/cicp.OA-2020-0099

Vol. **29**, No. 5, pp. 1446-1468
May 2021

A Highly Scalable Boundary Integral Equation and Walk-On-Spheres (BIE-WOS) Method for the Laplace Equation with Dirichlet Data

Changhao Yan[1,*], Wei Cai[2] and Xuan Zeng[1,*]

[1] *State Key Laboratory of ASIC and System, Fudan University,Shanghai, China.*
[2] *Department of Mathematics, Southern Methodist University, Dallas, TX 75275, USA.*

Received 6 May 2020; Accepted (in revised version) 24 September 2020

Abstract. In this paper, we study a highly scalable communication-free parallel domain boundary decomposition algorithm for the Laplace equation based on a hybrid method combining boundary integral equations and walk-on-spheres (BIE-WOS) method, which provides a numerical approximation of the Dirichlet-to-Neumann (DtN) mapping for the Laplace equation. The BIE-WOS is a local method on the boundary of the domain and does not require a structured mesh, and only needs a covering of the domain boundary by patches and a local mesh for each patch for a local BIE. A new version of the BIE-WOS method with second kind integral equations is introduced for better error controls. The effect of errors from the Feynman-Kac formula based path integral WOS method on the overall accuracy of the BIE-WOS method is analyzed for the BIEs, especially in the calculation of the right hand sides of the BIEs. For the special case of flat patches, it is shown that the second kind integral equation of BIE-WOS method can be simplified where the local BIE solutions can be given in closed forms. A key advantage of the parallel BIE-WOS method is the absence of communications during the computation of the DtN mapping on individual patches of the boundary, resulting in a complete independent computation using a large number of cluster nodes. In addition, the BIE-WOS has an intrinsic capability of fault tolerance for exascale computations. The nearly linear scalability of the parallel BIE-WOS method on a large-scale cluster with 6400 CPU cores is verified for computing the DtN mapping of exterior Laplace problems with Dirichlet data for several domains.

AMS subject classifications: 65C05, 65N99, 78M25, 92C45

Key words: Dirichlet-to-Neumann (DtN) mapping, meshless methods, parallel BIE-WOS method, Monte Carlo method, walk-on-spheres (WOS), boundary integral equations, Laplace equation, Dirichlet problem.

*Corresponding author. *Email addresses:* yanch@fudan.edu.cn (C. Yan), cai@smu.edu (W. Cai), xzeng@fudan.edu.cn (X. Zeng)

1 Introduction

The prevalence of many-core teraflops computing platforms makes scalability the principal concerns for developing new numerical algorithms for solving Laplace and Helmholtz equations, encountered in many engineering and scientific problems. Capacitance extractions of very large scale integral (VLSI) circuits in a full-chip, for example, solve the Laplace equation with Dirichlet boundary conditions in an extremely large scale. Boundary element methods (BEMs) or finite element methods (FEMs), widely used in capacitance extractions of VLSI circuits [2–7], are highly accurate and versatile, however, belonging to the deterministic and global methods, which need expensive surface or volume mesh generations of whole domains. Moreover, high scalability of BEMs and FEMs on millions of CPU cores is challenging in storing and solving large linear systems, prompting many research works [8, 9].

Random methods, based on Feynman-Kac probabilistic formula for the solutions, however, can offer local solutions of the Laplace equation [1,10–12] as well as natural parallelism. Potentials or charge densities are expressed as a weighted average of boundary Dirichlet data visited by multiple Brownian motion paths, sampled efficiently with the walk-on-spheres (WOS) method [23]. In fact, the industrial golden capacitance extraction tool QuickCap NX [13] is a practical example of such random methods [14, 15].

However, a naive application of the Feynman-Kac formula for the Dirichlet data is not applicable for an efficient calculation of the Neumann data on the boundary, as the Dirichlet boundary will absorb quickly the random particles starting near the boundary. To overcome such a drawback, we combined a deterministic boundary integral equation (BIE) and the probabilistic Feynman-Kac formula based walk-on-spheres (WOS) method, termed BIE-WOS [1], which allows us to compute the Neumann data over local patches of the domain boundary efficiently, while still maintaining the merit of natural parallelism of random methods. The BIE-WOS superimposes a hemisphere intersected with the boundary of interest and sets a local BIE over the subdomain enclosed by a part of the hemisphere and the intersected boundary. Using a homogeneous Green's function of a sphere results in the BIE involving only Dirichlet data over the hemisphere, which can be calculated by WOS algorithms. With the given Dirichlet data and unknown Neumann data on the patch surface, collocation methods can be employed to solve the integral equations on the aforementioned patch surface to yield the required Neumann data.

In this paper, we will present a new version of BIE-WOS with a well-conditioned integral equation of second kind (IESK), which has a much better error control related to the computation of the right hand side by the Feynman-Kac based WOS method. With the new IESK BIE-WOS, a highly scalable communication-free boundary domain decomposition BIE-WOS scheme is developed for the Laplace equation with Dirichlet data. The main highlights of this paper are summarized as follows. (1) First, we exam the original BIE-WOS method [1], which uses the integral equation of first kind (IEFK), even with its well-known ill-conditioned issue in the resulting linear systems, still much used in practice due to its simplicity. In fact, the first kind integral equation is still widely used in

capacitance extractions of VLSI circuits with high accuracy (with a maximal relative error $10^{-3}-10^{-4}$) [16,17]. However, we found some serious accuracy degeneration in the BIE-WOS method with the IEFK. The analysis will show that such an accuracy degeneration is not only attributed to the well-known ill-conditioning of the IEFK, but mainly to an amplification of errors, inevitably introduced by random methods of the BIE-WOS method, while computing the right hand side of the IEFK. It turns out that to avoid this error amplification, the proposed BIE-WOS method with the IESK is able to reduce the amplification of the random WOS-related errors in the calculation of the right hand side of the IESK, while still possessing a better conditioning of the IESK linear system. It is shown that BIE-WOS with the IESK is the preferred method for large parallel computations, even with the additional complexity of treating the hyper-singularity integrals involved. (2) Moreover, for the special case of a flat boundary patch, the BIE-WOS method with the IESK can be simplified with integrals evaluated in closed forms and can give the Neumann data on the flat patch directly, while the original BIE-WOS method in [1] can only give the Neumann data at a single point on a flat boundary. Meanwhile, we will show that the IESK with homogeneous Green's function of a sphere is equal to a natural BEM with a homogeneous three images Green's function of a hemisphere. Finally, we present the nearly linear scalability of the resulting parallel BIE-WOS on high-performance clusters with over 6400 CPU cores, for a maximal relative error 3.15% (acceptable for many real-world engineering applications).

The rest of the paper is organized as follows. The original BIE-WOS method is first briefly reviewed in Section 2. In Section 3, the new version of the BIE-WOS method with IESK is introduced while the integral kernels of both kind integral equations are given. Then, the special case of flat patches is discussed in detail. In Section 4, accuracy issues of the IEFK and IESK are analyzed for the case of flat patches. Numerical results are given in Section 5 while conclusions and discussions are given in Section 6.

2 Review of the BIE-WOS method

For an exterior domain $\Omega \subset R^3$, the solution of the Laplace equation

$$\begin{cases} -\Delta u = f, & \mathbf{x} \in \mathbf{\Omega}, \\ u|_{\partial\Omega} = \phi, \end{cases} \tag{2.1}$$

with $f = 0$, defines a mapping from the Dirichlet data u to the Neumann data $\frac{\partial u}{\partial \mathbf{n}}$ on the boundary $\partial\Omega$, i.e., a DtN mapping as follows,

$$\text{DtN:} \quad u|_{\partial\Omega} \to \left.\frac{\partial u}{\partial \mathbf{n}}\right|_{\partial\Omega}, \tag{2.2}$$

where $\mathbf{n}$ is the outward normal direction of boundary $\partial\Omega$.

Using the Green's second identity, the Neumann data at point $\mathbf{x}$ in the domain Ω is given as the solution of the following boundary integral equation of the first kind [30]

$$u(\mathbf{x}) = \int_{\partial\Omega} G(\mathbf{x},\mathbf{y}) \frac{\partial u(\mathbf{y})}{\partial \mathbf{n}_\mathbf{y}} ds_y - \int_{\partial\Omega} \frac{\partial G(\mathbf{x},\mathbf{y})}{\partial \mathbf{n}_\mathbf{y}} u(\mathbf{y}) ds_y, \quad \mathbf{x} \in \Omega, \tag{2.3}$$

where $\mathbf{n}_\mathbf{y}$ is the outward normal direction of boundary point $\mathbf{y}$, and $G(\mathbf{x},\mathbf{y})$ is the fundamental solution of Laplace operator in the free three-dimension space

$$G(\mathbf{x},\mathbf{y}) = \frac{1}{4\pi} \frac{1}{|\mathbf{x}-\mathbf{y}|}. \tag{2.4}$$

In order to solve (2.3), traditional BEMs discretize the whole boundary $\partial\Omega$ into small panels, construct a large dense linear system with collocation Nystrom methods, and then solve the resulting linear system for a numerical solution. The traditional BEMs are a global method as it is not possible to obtain just part of the Neumann data on the boundary as the BIE-WOS method proposed in [1].

The BIE-WOS method superimposes an imaginary hemisphere upon a relevant portion of the boundary $\partial\Omega$, where a *patch* S is the intersection of $\partial\Omega$ and the hemisphere, the hemispherical surface Γ is the outside part of the hemispherical surface exterior to domain Ω, and the shaded region bounded by $S \cup \Gamma$ is denoted as Ω_S.

Let $G_1(\mathbf{x},\mathbf{y})$ be the Green's function of a sphere with a homogeneous boundary condition on the whole sphere, which can be obtained easily using a Kelvin image, i.e.,

$$G_1(\mathbf{x},\mathbf{y}) = \frac{1}{4\pi} \left[\frac{1}{|\mathbf{x}-\mathbf{y}|} - \frac{a|\mathbf{y}|}{\left|a^2\mathbf{y} - |\mathbf{y}|^2\mathbf{x}\right|} \right], \tag{2.5}$$

where a is the radius of the hemisphere, the subscript 1 indicates one image charge is used in its definition, i.e. the term $\frac{1}{|\mathbf{x}-\mathbf{y}|}$ attributes to the source point inside the sphere, and the second term $\frac{-a|\mathbf{y}|}{\left|a^2\mathbf{y}-|\mathbf{y}|^2\mathbf{x}\right|}$ attributes to the image source outside the sphere.

Applying (2.3) to Ω_S, one can obtain for $\mathbf{x} \in \Omega_S$

$$u(\mathbf{x}) = -\int_\Gamma \frac{\partial G_1(\mathbf{x},\mathbf{y})}{\partial \mathbf{n}_\mathbf{y}} u(\mathbf{y}) ds_y + \int_S \left[-\frac{\partial G_1(\mathbf{x},\mathbf{y})}{\partial \mathbf{n}_\mathbf{y}} u(\mathbf{y}) + G_1(\mathbf{x},\mathbf{y}) \frac{\partial u(\mathbf{y})}{\partial \mathbf{n}_\mathbf{y}} \right] ds_y, \tag{2.6}$$

where $\int_\Gamma G_1(\mathbf{x},\mathbf{y}) \frac{\partial u(\mathbf{y})}{\partial \mathbf{n}_\mathbf{y}} ds_y = 0$, as G_1 vanishes on Γ by its homogeneous condition.

BIE (2.6) requires the solution value $u(\mathbf{y})|_\Gamma$, which will be calculated by the Feynman-Kac formula [19,20] and the WOS methods [18,21–25]. The Feynman-Kac formula gives a probabilistic solution $u(\mathbf{x})$ in (2.1) over a domain Ω with the Dirichlet boundary condition $\phi(\mathbf{x})$ as

$$u(\mathbf{x}) = E^x(\phi(X_{\tau_\Omega})) + E^x \left[\int_0^{\tau_\Omega} f(X_t) dt \right], \tag{2.7}$$

where the expectation is taken over all sampling paths $X_{t=0}(\omega)=\mathbf{x}$ and τ_Ω is the first hit time (or exit time) of the domain Ω. In this paper, we consider only for the Laplace equations ($f\equiv 0$).

On the patch S, both $u(\mathbf{y})$ and $\frac{\partial u(\mathbf{y})}{\partial \mathbf{n}}$ are involved, where $u(\mathbf{y})$ is given by the Dirichlet condition and $\frac{\partial u(\mathbf{y})}{\partial \mathbf{n}}$ is the unknown Neumann data to be calculated. Let $\mathbf{x}$ approaches the boundary S, the Neumann data $\frac{\partial u(\mathbf{y})}{\partial \mathbf{n}}$ over S can be solved with the following integral equation

$$K\left[\frac{\partial u}{\partial \mathbf{n}}\right](\mathbf{x})=b(\mathbf{x}),\quad \mathbf{x}\in S, \tag{2.8}$$

where

$$K\left[\frac{\partial u}{\partial \mathbf{n}}\right]\equiv\int_S G_1(\mathbf{x},\mathbf{y})\frac{\partial u(\mathbf{y})}{\partial \mathbf{n_y}}ds_y, \tag{2.9}$$

$$b(\mathbf{x})\equiv\left[\frac{u(\mathbf{x})}{2}+\text{p.v.}\int_S\frac{\partial G_1(\mathbf{x},\mathbf{y})}{\partial \mathbf{n_y}}u(\mathbf{y})ds_y\right]+\int_\Gamma\frac{\partial G_1(\mathbf{x},\mathbf{y})}{\partial \mathbf{n_y}}u(\mathbf{y})ds_y, \tag{2.10}$$

and here, p.v. stands for the Cauchy principal value of the double layer potential [26].

The integral equation (2.8), (2.9) and (2.10) is the first kind and ill-conditioned [17] with potential numerical difficulties. Differentiating on both sides of (2.6), one can obtain a well-conditioned second kind integral equation [27] as

$$\begin{aligned}\frac{\partial}{\partial \mathbf{n_x}}u(\mathbf{x})=&-\int_\Gamma\frac{\partial^2 G_1(\mathbf{x},\mathbf{y})}{\partial \mathbf{n_y}\partial \mathbf{n_x}}u(\mathbf{y})ds_y\\&+\int_S\left[-\frac{\partial^2 G_1(\mathbf{x},\mathbf{y})}{\partial \mathbf{n_y}\partial \mathbf{n_x}}u(\mathbf{y})+\frac{\partial G_1(\mathbf{x},\mathbf{y})}{\partial \mathbf{n_x}}\frac{\partial u(\mathbf{y})}{\partial \mathbf{n_y}}\right]ds_y,\quad \mathbf{x}\in\Omega_S.\end{aligned} \tag{2.11}$$

Now, let $\mathbf{x}$ approaches the boundary S, one obtains

$$\left(\frac{1}{2}I-D\right)\left[\frac{\partial u}{\partial \mathbf{n}}\right](\mathbf{x})=b(\mathbf{x}),\quad \mathbf{x}\in S, \tag{2.12}$$

where

$$D\left[\frac{\partial u}{\partial \mathbf{n}}\right](\mathbf{x})\equiv\text{p.v.}\int_S\frac{\partial G_1(\mathbf{x},\mathbf{y})}{\partial \mathbf{n_x}}\frac{\partial u(\mathbf{y})}{\partial \mathbf{n_y}}ds_y, \tag{2.13}$$

$$b(\mathbf{x})\equiv-\text{p.f.}\int_S\frac{\partial^2 G_1(\mathbf{x},\mathbf{y})}{\partial \mathbf{n_y}\partial \mathbf{n_x}}u(\mathbf{y})ds_y-\int_\Gamma\frac{\partial^2 G_1(\mathbf{x},\mathbf{y})}{\partial \mathbf{n_y}\partial \mathbf{n_x}}u(\mathbf{y})ds_y,\quad \mathbf{x}\in S, \tag{2.14}$$

where p.f. is the Hadamard finite part limit for the hyper-singular integral, which can be handled by various regularization techniques [26, 29].

3 BIE-WOS method with first and second kind integral equations

3.1 The integral kernels of the first and second integral equations in BIE-WOS

The BIE-WOS method can be formed with the first or second kind integral equations. With the first kind integral equation as (2.8), (2.9) and (2.10), the homogeneous Green's function is (2.5) and the first-order partial derivative of the Green's function in (2.10) is

$$\frac{\partial G_1(\mathbf{x},\mathbf{y})}{\partial \mathbf{n}_\mathbf{y}} = \frac{1}{4\pi}\begin{cases} \frac{|\mathbf{x}|^2-a^2}{ar^3}, & \mathbf{y}\in\Gamma, \\ -\frac{\mathbf{r}\cdot\mathbf{n}_\mathbf{y}}{r^3}+\frac{a(|\mathbf{x}|^2\mathbf{y}-a^2\mathbf{x})}{T^3}\cdot\mathbf{n}_\mathbf{y}, & \mathbf{y}\in S, \end{cases} \tag{3.1}$$

where $\mathbf{r}=\mathbf{x}-\mathbf{y}$, $r=|\mathbf{x}-\mathbf{y}|$, $T=\sqrt{a^4-2a^2(\mathbf{x}\cdot\mathbf{y})+|\mathbf{x}|^2|\mathbf{y}|^2}$, and a is the radius of the hemisphere.

If $\mathbf{x}$ and $\mathbf{y}$ coincide, (2.5) becomes weakly singular while (3.1) becomes strongly singular. Fortunately, both singularities can be easily regularized by polar coordinate transform [26,28].

If the BIE-WOS method is formed with the second kind integral equation as (2.12), (2.13) and (2.14), the first-order partial derivative of the Green's function in (2.13) is

$$\begin{aligned} &\frac{\partial G_1(\mathbf{x},\mathbf{y})}{\partial \mathbf{n}_\mathbf{x}} = \frac{1}{4\pi}[G_I+G_{II}]\cdot\mathbf{n}_\mathbf{x}, \\ &G_I=\frac{\mathbf{r}}{r^3}, \quad G_{II}=\frac{a(|\mathbf{y}|^2\mathbf{x}-a^2\mathbf{y})}{T^3}, \end{aligned} \tag{3.2}$$

where $\mathbf{x}=\{x_1,x_2,x_3\}$, $\mathbf{y}=\{y_1,y_2,y_3\}$, $\mathbf{x}\cdot\mathbf{y}=x_1y_1+x_2y_2+x_3y_3$, $T=\sqrt{a^4-2a^2(\mathbf{x}\cdot\mathbf{y})+|\mathbf{x}|^2|\mathbf{y}|^2}$, $r=|\mathbf{r}|$, $\mathbf{r}=\mathbf{x}-\mathbf{y}$.

If $\mathbf{x}$ and $\mathbf{y}$ coincide, (3.2) is a strongly singular integral for the first term $\frac{\mathbf{r}}{r^3}$, and the second term $\frac{a(|\mathbf{x}|^2\mathbf{y}-a^2\mathbf{x})}{T^3}$ in (3.2) has no singularity, because T is always larger than zero. However, it becomes a nearly strong singularity when point $\mathbf{x}$ approaches to the hemisphere surface.

Meanwhile, the second-order partial derivative of the Green's function in (2.14) is

$$\frac{\partial^2 G_1(\mathbf{x},\mathbf{y})}{\partial \mathbf{n}_\mathbf{y}\partial \mathbf{n}_\mathbf{x}} = \begin{cases} \mathbf{n}_\mathbf{x}\cdot H_1, & \mathbf{y}\in\Gamma, \\ \mathbf{n}_\mathbf{y}\cdot[\overline{G}_I+\overline{G}_{II}]\cdot\mathbf{n}_\mathbf{x}, & \mathbf{y}\in S, \end{cases} \tag{3.3}$$

where the Einstein's notation is introduced, and

$$H_1 = -\frac{1}{4\pi}\frac{1}{ar^5}\left[3\mathbf{y}\circ(a^2-|\mathbf{x}|^2+\mathbf{x}\circ\mathbf{x})+\mathbf{x}\circ(-5a^2+4\mathbf{x}\cdot\mathbf{y}+|\mathbf{x}|^2-3\mathbf{x}\circ\mathbf{y})\right], \tag{3.4}$$

$$\overline{G}_I = \frac{1}{r^3}\left(\delta_{ij}-3\frac{r_i r_j}{r^2}\right), \tag{3.5}$$

$$\overline{G}_{II} = \begin{cases} -\frac{a(a^2+\mathbf{x}\circ\mathbf{y})}{T^3}+\frac{3a^3(|\mathbf{y}|^2\mathbf{x}\circ\mathbf{x}-2(\mathbf{x}\cdot\mathbf{y})\mathbf{x}\circ\mathbf{y}+|\mathbf{x}|^2\mathbf{y}\circ\mathbf{y})}{T^5}, & i=j, \\ \frac{2ay_ix_j}{T^3}-\frac{3a}{T^5}\left[y_ix_ja^4-a^2(x_ix_j|\mathbf{y}|^2+y_iy_j|\mathbf{x}|^2)+y_jx_i|\mathbf{x}|^2|\mathbf{y}|^2\right], & i\neq j, \end{cases} \tag{3.6}$$

where δ_{ij} is a 3×3 identity matrix, and $\circ$ denotes the Hadamard product, namely, $\mathbf{x}\circ\mathbf{y}=\{x_1y_1,x_2y_2,x_3y_3\}$, and the inner product $\mathbf{x}\cdot\mathbf{y}=x_1y_1+x_2y_2+x_3y_3$, $T=\sqrt{a^4-2a^2(\mathbf{x}\cdot\mathbf{y})+|\mathbf{x}|^2|\mathbf{y}|^2}$.

If $\mathbf{y}\in\mathbf{\Gamma}$, (3.4) has no singularity because $\mathbf{x}$ is on the patch S, and therefore r is always larger than zero. However, it will be nearly singular when $\mathbf{x}$ is near the intersection edge $\Gamma\cap S$.

If $\mathbf{y}\in\mathbf{S}$, $\overline{G}_I$ is hyper-singular when $\mathbf{x}$ and $\mathbf{y}$ coincide, which can be regularized by the methods in [29]. At these situations, $\overline{G}_{II}$ has no singularity as T is always larger than zero. However, $\overline{G}_{II}$ becomes nearly singular when $\mathbf{x}$ is near to the intersection edge $\Gamma\cap S$. Note that both $\overline{G}_I$ and $\overline{G}_{II}$ are 3x3 matrices. When $\mathbf{y}\in S$, $\overline{G}_I$ is a symmetric matrix, while $\overline{G}_{II}$ is not.

3.2 Simplification for flat surface patches on the boundary

For a small patch S on smooth part of the boundary, the patch S can be approximated by a flat one without sacrificing much of the overall accuracy. Then, when both $\mathbf{x}$ and $\mathbf{y}$ are on S, we have $\mathbf{x}\cdot\mathbf{n}_\mathbf{x}=\mathbf{y}\cdot\mathbf{n}_\mathbf{x}=\mathbf{r}\cdot\mathbf{n}_\mathbf{x}=0$, $y_3=0$ and $\mathbf{n}_\mathbf{y}=\mathbf{n}_\mathbf{x}=\{0,0,-1\}$ under the local coordinate on patch S. Therefore, all integral kernels of the first and second kind in the BIE-WOS algorithm can be simplified.

Applying (3.1) into the first kind integral equation of the BIE-WOS (2.8), for $\mathbf{y}\in S$, then

$$\text{p.v.}\int_S \frac{\partial G_1(\mathbf{x},\mathbf{y})}{\partial\mathbf{n}_\mathbf{y}}u(\mathbf{y})ds_y = \text{p.v.}\int_S\left[-\frac{\mathbf{r}\cdot\mathbf{n}_\mathbf{y}}{r^3}+\frac{a(|\mathbf{x}|^2\mathbf{y}-a^2\mathbf{x})}{T^3}\cdot\mathbf{n}_\mathbf{y}\right]u(\mathbf{y})ds_y = 0,$$

where the first term $-\frac{\mathbf{r}\cdot\mathbf{n}_\mathbf{y}}{r^3}$ is a strong singular integral, and its Cauchy principal is zero as the jump term $1/2$ on smooth boundary has already been taken out in (2.8), and the second term $\frac{a(|\mathbf{x}|^2\mathbf{y}-a^2\mathbf{x})}{T^3}\cdot\mathbf{n}_\mathbf{y}$ is zero as it has no singularity.

Therefore, the first kind integral equation of the BIE-WOS (2.8) can be simplified as

$$\int_S G_1(\mathbf{x},\mathbf{y})\frac{\partial u(\mathbf{y})}{\partial\mathbf{n}_\mathbf{y}}ds_y = \frac{u(\mathbf{x})}{2}+\int_\Gamma\frac{\partial G_1(\mathbf{x},\mathbf{y})}{\partial\mathbf{n}_\mathbf{y}}u(\mathbf{y})ds_y, \quad \mathbf{x}\in S. \tag{3.7}$$

All steps for constructing the linear system, the discretization of the flat patch in the scheme of BIE are still required.

The second kind integral equation of the BIE-WOS (2.12) can be simplified more. Considering the fact that when both $\mathbf{x}$ and $\mathbf{y}$ are on S,

$$\begin{aligned} D\left[\frac{\partial u}{\partial \mathbf{n}}\right](\mathbf{x}) &= \text{p.v.}\int_S \frac{\partial G_1(\mathbf{x},\mathbf{y})}{\partial \mathbf{n}_\mathbf{x}}\frac{\partial u(\mathbf{y})}{\partial \mathbf{n}_\mathbf{y}}ds_y \\ &= \text{p.v.}\int_S \frac{1}{4\pi}[G_I+G_{II}]\cdot\mathbf{n}_\mathbf{x}\frac{\partial u(\mathbf{y})}{\partial \mathbf{n}_\mathbf{y}}ds_y = 0, \end{aligned} \tag{3.8}$$

where again the Cauchy principal integral of the first term $G_I\cdot\mathbf{n}_\mathbf{x}=\frac{\mathbf{r}}{r^3}\cdot\mathbf{n}_\mathbf{x}$ is zero as the jump term $1/2$ on smooth boundary has already been taken out in (2.12), and the second term $G_{II}\cdot\mathbf{n}_\mathbf{x}=\frac{a(y^2\mathbf{x}-a^2\mathbf{y})}{T^3}\cdot\mathbf{n}_\mathbf{x}$ is zero as it has no singularity.

Plugging (3.8) into (2.12), we obtain

$$\left[\frac{\partial u}{\partial \mathbf{n}}\right](\mathbf{x}) = -2\left[\int_\Gamma \frac{\partial^2 G_1(\mathbf{x},\mathbf{y})}{\partial \mathbf{n}_\mathbf{y}\partial \mathbf{n}_\mathbf{x}}u(\mathbf{y})ds_y + \text{p.f.}\int_S \frac{\partial^2 G_1(\mathbf{x},\mathbf{y})}{\partial \mathbf{n}_\mathbf{y}\partial \mathbf{n}_\mathbf{x}}u(\mathbf{y})ds_y\right], \quad \mathbf{x}\in S, \tag{3.9}$$

where

$$\frac{\partial^2 G_1(\mathbf{x},\mathbf{y})}{\partial \mathbf{n}_\mathbf{y}\partial \mathbf{n}_\mathbf{x}} = \begin{cases} \frac{1}{4\pi}\frac{3y_3\left[a^2-{\rho_x}^2\right]}{a\left[a^2+{\rho_x}^2-2(x_1y_1+x_2y_2)\right]^{5/2}}, & \mathbf{y}\in\Gamma, \\ \frac{1}{4\pi}\left[\frac{1}{r^3}-\frac{a^3}{\left(\rho_y r_I\right)^3}\right], & \mathbf{y}\in S, \end{cases} \tag{3.10}$$

with $\mathbf{x}=\{x_1,x_2,x_3\}$, $\mathbf{y}=\{y_1,y_2,y_3\}$, $\mathbf{y_I}=k\mathbf{y}$, $k=\frac{a^2}{\rho_y^2}$, $r=|\mathbf{y}-\mathbf{x}|$, $r_I=|\mathbf{y_I}-\mathbf{x}|$, $\rho_x=\sqrt{{x_1}^2+{x_2}^2}$, $\rho_y=\sqrt{{y_1}^2+{y_2}^2}$.

Based on (3.9) and (3.10), the second kind integral equation of BIE-WOS is simplified as an explicit integral, which can be calculated directly by the numerical quadrature on Γ and S. The potentials $u(\mathbf{y})$ on S are given by the Dirichlet boundary condition, and $u(\mathbf{y})$ on Γ is calculated by the WOS algorithm. All the discretization of the flat patch, numerical implementations of the BIE, solutions of the linear system will be unnecessary.

When $\mathbf{y}\in\Gamma$, (3.9) and (3.10) have no singularity because the denominator is always larger than zero. However, (3.10) becomes nearly hyper-singular, when x approaches the edge $\Gamma\cap S$. When $\mathbf{y}\in S$, (3.10) includes two parts $\frac{1}{r^3}$ and $\frac{a^3}{(\rho_y r_I)^3}$. The first part $\frac{1}{r^3}$ has an hyper-singularity when x and y coincide, but it can be regularized by methods in [26,29]. The second part $\frac{a^3}{(\rho_y r_I)^3}$ has no singularity, but again has nearly hyper-singularity when x approaches the edge $\Gamma\cap S$.

Remark 3.1 (Connection with Indirect BEM)**.** In fact, we can deduce the same results of (3.9) and (3.10) from the indirect BEM [30]. For a hemisphere Γ, the homogeneous Green's function $G_1(\mathbf{x},\mathbf{y})$ in (3.9) and (3.10) is the Green's function with one image charge.

For a half-ball domain Ω_{hb}, i.e. $\partial\Omega_{hb}=\Gamma\cup S$, the Neumann solution can be obtained directly by the indirect BEM as

$$\frac{\partial u(\mathbf{x})}{\partial \mathbf{n}_{\mathbf{x}}}=-\int_{\partial\Omega}\frac{\partial^2 G_3(\mathbf{x},\mathbf{y})}{\partial \mathbf{n}_{\mathbf{y}}\partial \mathbf{n}_{\mathbf{x}}}u(\mathbf{y})ds_y, \tag{3.11}$$

where the homogeneous Green's function of a half-ball $G_3(\mathbf{x},\mathbf{y})$ is the three images Green's function, i.e.,

$$G_3(\mathbf{x},\mathbf{y})=\frac{1}{4\pi}[g_0(\mathbf{x},\mathbf{y})+g_1(\mathbf{x},\mathbf{y})+g_2(\mathbf{x},\mathbf{y})+g_3(\mathbf{x},\mathbf{y})], \tag{3.12}$$

where $\mathbf{x}=\{x_1,x_2,x_3\}$, $\mathbf{y}=\{y_1,y_2,y_3\}$, $\gamma=a^2/|\mathbf{x}|^2$, three images are defined as $\mathbf{x}^{(1)}=\gamma\mathbf{x}$, $\mathbf{x}^{(2)}=\{x_1,x_2,-x_3\}$, $\mathbf{x}^{(3)}=\{x_1^{(1)},x_2^{(1)},-x_3^{(1)}\}$, and $g_0(\mathbf{x},\mathbf{y})=1/r(\mathbf{y},\mathbf{x})$, $g_1(\mathbf{x},\mathbf{y})=-a/|\mathbf{x}|/r(\mathbf{y},\mathbf{x}^{(1)})$, $g_2(\mathbf{x},\mathbf{y})=-1/r(\mathbf{y},\mathbf{x}^{(2)})$, $g_3(\mathbf{x},\mathbf{y})=a/|\mathbf{x}|/r(\mathbf{y},\mathbf{x}^{(3)})$, $r(\mathbf{x},\mathbf{y})=|\mathbf{x}-\mathbf{y}|$.

We can show that

$$\frac{\partial^2 G_3(\mathbf{x},\mathbf{y})}{\partial \mathbf{n}_{\mathbf{x}}\partial \mathbf{n}_{\mathbf{y}}}=2\frac{\partial^2 G_1(\mathbf{x},\mathbf{y})}{\partial \mathbf{n}_{\mathbf{x}}\partial \mathbf{n}_{\mathbf{y}}}. \tag{3.13}$$

Therefore, (3.9) is the same as (3.11) indeed.

Remark 3.2. (1) The key advantage of the second kind of integral equation in (3.9) and (3.10) for a flat patch is that the Neumann data is given directly by an explicit formula, and only the WOS method for potentials on the hemisphere and numerical quadratures are needed. Therefore, compared with the method on a curve patch, there is no discretization of the patch and no coding for the BEM, thus the implementation is much simplified. (2) The flat patch S is only a local assumption where the fictitious hemisphere intersects with the boundary $\partial\Omega$. Therefore, such constraint can be easily satisfied or approximated for many engineering applications, where the surface is not too rough. (3) In the original BIE-WOS method [1], the integral $\Sigma_1=-\int_\Gamma\frac{\partial^2 G(\mathbf{x},\mathbf{y})}{\partial \mathbf{n}_{\mathbf{x}}\partial \mathbf{n}_{\mathbf{y}}}u(\mathbf{y})ds_y=-\int_\Gamma(\frac{3}{2\pi}\frac{\cos\theta}{a^3})u(\mathbf{y})ds_y$ of (3.13) and the integral $\Sigma_2=-\text{p.f.}\int_{S_a}\frac{\partial^2 G(\mathbf{x},\mathbf{y})}{\partial \mathbf{n}_{\mathbf{x}}\partial \mathbf{n}_{\mathbf{y}}}u(\mathbf{y})ds_y=-\text{p.f.}\int_{S_a}\frac{1}{2\pi}(\frac{1}{\rho^3}-\frac{1}{a^3})u(\mathbf{y})ds_y$ of (5.1) are the special cases of (3.9) and (3.10) proposed in this paper. Following (3.13) and (5.1) in the original BIE-WOS [1], only the Neumann data at the center of the hemisphere can be calculated. In (3.9) and (3.10) of this paper, however, all Neumann data on the flat patch can be obtained with nearly the same costs, as calculating potentials on the hemisphere by the WOS method dominates the total CPU time, and numerical quadrature cost is low.

4 Effect of error for the right hand side of IEFK and IESK in BIE-WOS methods

In general, BIE/BEM methods can achieve satisfactory accuracy for engineering applications ($10^{-3}-10^{-5}$). However, we observed an unusual accuracy degeneration for the

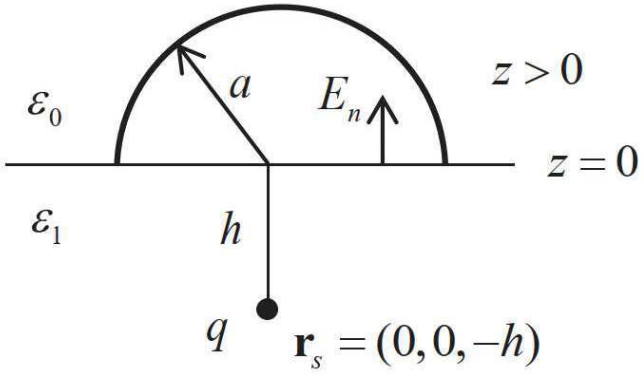

Figure 1: Two dielectric half-plane separated by the planar interface $z=0$.

BIE-WOS method with IEFK, while the one with IESK maintains good accuracy. Such an accuracy discrepancy between the first and second kind integral is partly attributed to the well-known fact that IEFK is ill-conditioned while the IESK is well-conditioned [17]. But a closer examination shows that the ill-conditioning of the linear system (matrix A) does not explain the whole reason of the accuracy degeneration of the BIE-WOS method with the IEFK. The major cause in fact is on the computation of the right-hand side of the BIEs where an adversary error amplification could occur in the case of IEFK. In this section, we first exam the phenomenon of the accuracy degeneration in IEFK of BIE-WOS, then analyze the reasons in detail.

A simple half-plane test case is given in Fig. 1, where the plane $z=0$ divides the space into two dielectric domains with dielectric constants ϵ_0 and ϵ_1, respectively. A unit charge q is located at $\mathbf{r}_s=(0,0,-h)$. The Neumann data on plane $z=0$ is to be calculated. The potential $u(\mathbf{r})$ for the upper domain $z>0$ satisfies the Laplace equation $\nabla^2 u(\mathbf{r})=0$, with variable Dirichlet data on the boundary $z=0$. The analytic solution of potentials and Neumann data on $z=0$ are given as

$$u(\mathbf{r})=\frac{q'}{4\pi\epsilon_0}\frac{1}{|\mathbf{r}-\mathbf{r}_s|},\frac{\partial u(\mathbf{r})}{\partial n}=\frac{q'}{4\pi\epsilon_0}\frac{-(\mathbf{r}-\mathbf{r}_s)\cdot\{0,0,-1\}}{|\mathbf{r}-\mathbf{r}_s|^3},\quad q'=\frac{2\epsilon_0}{\epsilon_0+\epsilon_1}q. \tag{4.1}$$

Following the BIE-WOS method, a hemisphere with radius $a=1$ is constructed centered at $o=(0,0,0)$. A classic collocation and linear BEM is applied for the first kind integral equation in (3.7), (2.5) and (3.1), and for the second kind one in (3.9) and (3.10).

We change the distance h of the charge q with h =1,10,20,50 and 100, respectively. Fig. 2 gives the relative errors of all discretized panels within the radius 0.7a for avoiding the *corner effect* [17], where Fig. 2(a,b) and Fig. 2(c,d) are for IEFK and IESK, respectively. Meanwhile, the details of the condition numbers and maximal relative errors of all linear systems are listed in Table 1.

The matrix size of linear systems $Ax=b$ of IEFK's and IESK's in this case is 1513×1513, and the discretizations of both IEFK and IESK are the same. From the results, we can see

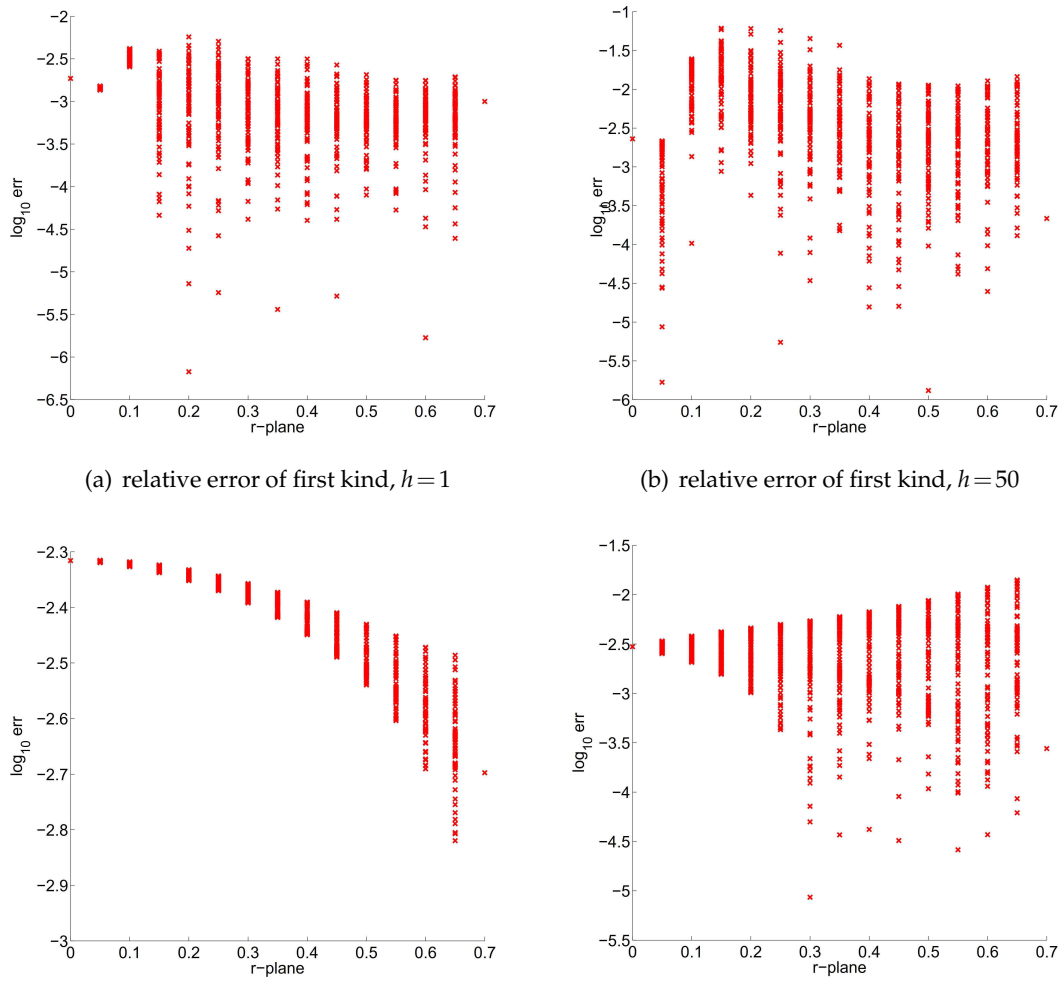

(a) relative error of first kind, $h=1$

(b) relative error of first kind, $h=50$

(c) relative error of second kind, $h=1$

(d) relative error of second kind, $h=50$

Figure 2: Accuracy comparison of the integral equations of first (IEFK) and second (IESK) kinds.

that as the charge distance h increases from 1 to 100, the maximal relative errors of IEFK's increase from 0.57% to 13.82%, while the errors of IESK's only increase from 0.47% to 1.41%. $cond(A)$ in Table 1 verifies the ill-conditioning of the IEFK (358.5) and IESK is well-conditioned (1), however, it is not the reason for IEFK's accuracy degeneration. When the charge distance h increases from 1 to 100, the matrices A of IEFK's and the condition numbers of A remain the same, therefore, they can not explain the huge difference of accuracy degeneration from 0.57% to 13.82%. However, for different h, the right hand sides of the matrix system will change and we will see this is indeed the cause of the different accuracy patterns for the BIE-WOS method with IEFK and IESK.

Table 1: Comparison of condition numbers and accuracies between integral equation of the first (IEFK) and second (IESK) kinds.

h	max relative error(%) of IEFK cond(A)=358.5	max relative error(%) of IESK cond(A)=1
1	0.57	0.48
10	2.81	0.47
20	4.09	0.81
50	6.11	1.41
100	13.82	1.39

It is expected that a condition number 358.5 will result in a loss of 2-3 significant digits in the numerical results, usually acceptable for engineering applications. For example, the Fastcap [4], a capacitance extraction software in 3D VLSI circuits with the first kind BIE method, can easily achieve high accuracy (with a maximal relative error $10^{-3}-10^{-4}$). The loss of significant digits of IEFK is not mainly due to the large condition number the matrix A in the linear system $Ax=b$, but more to the calculation of the right-hand b, where a large error amplification occurred.

Considering the fact

$$\int_{S\cup\Gamma}\frac{\partial^2 G_1(\mathbf{x},\mathbf{y})}{\partial\mathbf{n}_\mathbf{y}\partial\mathbf{n}_\mathbf{x}}c(\mathbf{x})ds_y\equiv 0, \tag{4.2}$$

where $c(\mathbf{x})$ is any constant function of $\mathbf{x}$, the right hand of IESK (2.14) can be rewritten as

$$b(\mathbf{x})\equiv \text{p.f.}\int_S\frac{\partial^2 G_1(\mathbf{x},\mathbf{y})}{\partial\mathbf{n}_\mathbf{y}\partial\mathbf{n}_\mathbf{x}}[c(\mathbf{x})-u(\mathbf{y})]ds_y+\int_\Gamma\frac{\partial^2 G_1(\mathbf{x},\mathbf{y})}{\partial\mathbf{n}_\mathbf{y}\partial\mathbf{n}_\mathbf{x}}[c(\mathbf{x})-u(\mathbf{y})]ds_y,\quad \mathbf{x}\in S. \tag{4.3}$$

We can set $c(\mathbf{x})=u(\mathbf{x})$ to reduce the singularity when $\mathbf{y}$ is near to $\mathbf{x}$ on S [1].

Therefore, the right-hand b of both the IEFK and IESK can be summarized as

$$b(\mathbf{x})=\int_S(\,)\cdot u(\mathbf{y})ds_y+\int_\Gamma(\,)\cdot u(\mathbf{y})ds_y=b_S(\mathbf{x})+b_\Gamma(\mathbf{x}), \tag{4.4}$$

$$b_S(\mathbf{x})=\sum_i w_{1,i}(\mathbf{x},y_i)u(y_i),\quad b_\Gamma(\mathbf{x})=\sum_i w_{2,i}(\mathbf{x},y_i)u(y_i), \tag{4.5}$$

where b_S, b_Γ are integrals on the flat patch S and hemisphere Γ, respectively, and $w_{1,i}(\mathbf{x},y_i)$ and $w_{2,i}(\mathbf{x},y_i)$ include different integral kernels and weights of the Gauss quadrature, and i is the index of integration quadrature points.

While the Dirichlet data $u(\mathbf{y})$ on the flat patch S is known without errors, the data $u(\mathbf{y})$ on the hemisphere Γ, however, has to be calculated by the random walk WOS in the BIE-WOS method. BIE-WOS methods require large amount of Brownian path samples for a satisfactory accuracy, due to the convergence rate of the $\mathcal{O}(1/\sqrt{N})$ for N paths. In the half-plane case, for example, the maximal relative error of $u|_\Gamma$ by WOS is about 0.5%−

1% for $N = 5\times10^5$ paths. The accuracy of numerical quadrature, however, is usually $10^{-4}-10^{-6}$, thus, having no adversary effect on the overall accuracy. Therefore, we only need to exam the error introduced by the WOS method, say,

$$\widetilde{u}(\mathbf{y})=[1+\delta_r(\mathbf{y})]u(\mathbf{y}),\quad \mathbf{y}\in\Gamma, \tag{4.6}$$

where $u(\mathbf{y})$ is the true potential on point $\mathbf{y}$, $\widetilde{u}(\mathbf{y})$ is the potential calculated by the random WOS methods, and $\delta_r(\mathbf{y})$ is the relative error of the WOS solution.

For the simplicity of argument, let us assume that $u(\mathbf{y})\geq 0$, $\mathbf{y}\in\Gamma$, then

$$\begin{aligned}|\widetilde{b}_\Gamma(\mathbf{x})|&=\sum_i w_{2,i}(\mathbf{x},y_i)[1+\delta_r(y_i)]u(y_i)\\&\leq(1+|\delta_{r,\max}|)\sum_i w_{2,i}(\mathbf{x},y_i)u(y_i)\\&\leq(1+|\delta_{r,\max}|)|b_\Gamma(\mathbf{x})|,\end{aligned} \tag{4.7}$$

where $|\delta_{r,\max}|=\max_i|\delta_r(y_i)|$.

Therefore, the relative error of right hand $\delta_b(\mathbf{x})$ is

$$|\delta_b(\mathbf{x})|=\left|\frac{b_s(\mathbf{x})+\widetilde{b}_\Gamma(\mathbf{x})}{b_s(\mathbf{x})+b_\Gamma(\mathbf{x})}-1\right|\leq\left|\frac{1}{\frac{b_s(\mathbf{x})}{b_\Gamma(\mathbf{x})}+1}\right||\delta_{r,\max}|=f\Big(\frac{b_s(\mathbf{x})}{b_\Gamma(\mathbf{x})}\Big)|\delta_{r,\max}|, \tag{4.8}$$

where an amplification function $f(z)$ is defined as

$$f(z)=\frac{1}{z+1}. \tag{4.9}$$

One can clearly see that if the signs of $b_S(\mathbf{x})$ and $b_\Gamma(\mathbf{x})$ are the same, i.e. $z=\frac{b_s(\mathbf{x})}{b_\Gamma(\mathbf{x})}\geqslant 0$, the relative error of right hand $|\delta_b(\mathbf{x})|\leqslant|\mathbf{ffi}_{\mathbf{r},\max}|$. However, if the signs of $b_S(\mathbf{x})$ and $b_\Gamma(\mathbf{x})$ are different, i.e. $z\leqslant 0$, the upper bound of the relative error of right hand will be amplified. Especially, if $b_S(\mathbf{x})\approx -b_\Gamma(\mathbf{x})$, i.e. $z\approx -1$, a large error amplification occurs as $|f(z)|\gg 1$.

As a result of the behavior of the amplification function $f(z)$, on a flat patch surface S, for the IEFK of BIE-WOS, assuming $u(\mathbf{x})\geqslant 0$,

$$b_S(\mathbf{x})=\frac{u(\mathbf{x})}{2}>0, \tag{4.10}$$

$$b_\Gamma(\mathbf{x})=\int_\Gamma(\frac{x^2-a^2}{ar^3})u(\mathbf{y})ds_y<0. \tag{4.11}$$

Therefore, as discussed above, IEFK will lose accuracy as the upper bound of the relative error of right hand will be enlarged with $z=\frac{b_s(\mathbf{x})}{b_\Gamma(\mathbf{x})}<0$ and $|f(z)|\geqslant 1$ if the absolute values of $b_S(\mathbf{x})$ and $\widetilde{b}_\Gamma(\mathbf{x})$ are similar, it has a large adversary effect on the overall accuracy of the solution, which is exactly what happened for the case of the half-plane with $h=50$.

On the other hand, for the IESK of BIE-WOS with large c(x), we can show that

$$b_S(\mathbf{x}) = \text{p.f.} \int_S \frac{1}{4\pi} \left[\frac{1}{r^3} - \frac{a^3}{\left(\rho_y r_I\right)^3} \right] [c(\mathbf{x}) - u(\mathbf{y})]\, ds_y > 0, \tag{4.12}$$

$$\widetilde{b}_\Gamma(\mathbf{x}) = \int_\Gamma \frac{1}{4\pi} \frac{3y_3 \left[a^2 - {\rho_x}^2\right]}{a[a^2 + {\rho_x}^2 - 2(x_1 y_1 + x_2 y_2)]^{5/2}} [c(\mathbf{x}) - u(\mathbf{y})]\, ds_y > 0. \tag{4.13}$$

Therefore, IESK will behave better in terms of error amplification in the calculation of the right hand side, for $z = \frac{b_s(\mathbf{x})}{b_\Gamma(\mathbf{x})} \geqslant 0$ and the relative error of right-hand $\delta_b \leqslant \delta_{r,\max}$. For the extreme case with $h = 50$, $\delta_b \approx \delta_{r,\max}$ and $x \approx 0$, i.e., the relative error of the final results is dominated by WOS methods. Certainly, the trade-off is that we need to handle the higher singularities (hyper-singularity and near hyper-singularity) in the integral kernels for the IESK.

Fig. 3 verifies the above observations for various components of the right-hand b for different h. The x-axis is the index of the discretized panels, and y-axis is $b_S(\mathbf{x})$, $\widetilde{b}_\Gamma(\mathbf{x})$, and $b(\mathbf{x})$ of the panels. From Fig. 3, one can see that when h varies from 1 to 50, for IEFK, $b_S(\mathbf{x}) > 0$, $b_\Gamma(\mathbf{x}) < 0$, $b(\mathbf{x})$ is near to zero when $h = 50$, and there are huge errors on $b(\mathbf{x})$, because of the numerical cancelation. For the IESK, however, both $b_S(\mathbf{x}) > 0$ and $b_\Gamma(\mathbf{x}) > 0$, therefore total $b(\mathbf{x}) > 0$ and there is no cancelation on $b(\mathbf{x})$.

Remark 4.1. (1) The error of right hand side $f(\frac{b_s(\mathbf{x})}{b_\Gamma(\mathbf{x})})\delta_{r,\max}$ includes two parts. The source of error $\delta_{r,\max}$, induced by discretization errors, numerical quadratures, random walks, etc., is only dependent on the geometry of boundary, and is independent of the Dirichlet data on the boundary. The amplification factor $f(\frac{b_s(\mathbf{x})}{b_\Gamma(\mathbf{x})})$ is not a numerical error source and dependent on the exact solution, related to the boundary geometry and Dirichlet data. Therefore, in this case, when distance h changes, the Dirichlet data changes and the amplification factor changes correspondingly. Meanwhile the error sources from the numerical quadratures, random walks are unchanged. (2) Basically, the integral kernels of IEFK has its right hand side as the difference between $b_s(\mathbf{x})$ and $|b_\Gamma(\mathbf{x})|$, so cancelation is essentially inside and amplification factor is always larger than 1. In traditional BEMs with IEFK, such a phenomenon is not easily observed, because the accuracy of right-hands, resulting from numerical quadratures, is usually high enough (10^{-4}). (3) The right-hands of IESK are additive, so the amplification factor is less than 1, thus numerically stable. In the BIE-WOS method, the IESK is highly recommended as its relative error of the right hand is not enlarged with the inevitable and hard-to-reduce error in the order of 10^{-2} introduced by the WOS method. However, special treatments are needed for more complicated integral kernels, higher singularity with more complicate regularized methods. (4) The IEFK in the BIE-WOS method should be applied in a careful manner, where $\widetilde{b}$, b_S, $\widetilde{b}_\Gamma$ must be compared to avoid accepting the results under numerical cancelations and error amplifications. For general cases, the criterion for applying the IEFK with confidence needs further studies.

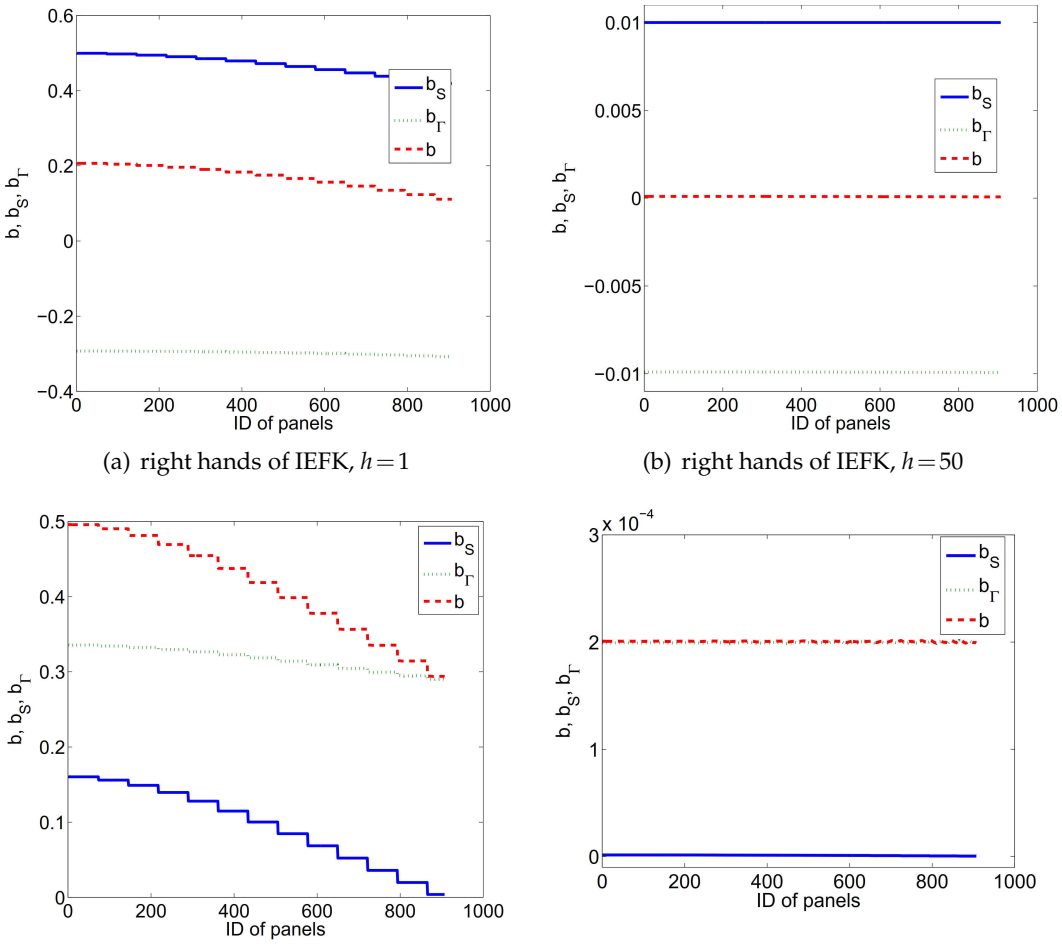

(a) right hands of IEFK, $h=1$

(b) right hands of IEFK, $h=50$

(c) right hands of IESK, $h=1$

(d) right hands of IESK, $h=50$

Figure 3: Comparisons of right-hand b_S, b_Γ, b for the first and second kind integral equations.

5 Numerical results

5.1 The algorithm of the parallel BIE-WOS method

The scheme of the parallel BIE-WOS method is straightforward. For a large domain where the exterior Laplace equation solution to be found, many hemispheres are superimposed to cover the Neumann data surface, and the DtN mapping on the patch of boundary intersected by each hemisphere is solved independently by the BIE-WOS method. Therefore, it is a highly scalable boundary domain decomposition method for a communication-free among hemispheres and allows the natural parallel implementation of the random walks for the problem for each hemisphere. Also, the radius of hemispheres can be different, and the local patches of the hemisphere are preferably

overlapped. It is evident no global structured surface mesh is required for the parallel BIE-WOS method and only a local mesh on each patch is needed for the BIEs.

5.2 Accuracy and scalability of the parallel BIE-WOS method

Several large scale tests are presented below to demonstrate the accuracy and parallel efficiency of the proposed parallel BIE-WOS method. The parallel BIE-WOS algorithm is implemented in C/C++ language with the openMP [31] and MPI [32] for a large scale parallel computation on high-performance clusters. In the MPI implementation, a master node dispatches tasks of individual hemisphere to idle computational nodes and collect results. Each computational node is accelerated by the openMP for WOS sampling of the Brownian paths and quadratures of all integrals.

The parallel efficiency of the proposed method is tested under the *weak scalability*, i.e., the task loads increasing as the CPU cores increasing. For example, we use 32 CPU nodes for the 32x task load and 256 CPU nodes for the 256x task load, where the 32x and 256X task load has 32 and 256 hemispheres to cover parts of the whole surface, respectively. Therefore, different problems are solved indeed each time with different CPU nodes. Thus, the accuracies are correspondingly the maximal relative error for different problems which has a different task load, thus the difference in accuracy. Experiment results verify the high scalability of the BIE-WOS algorithms.

On each hemisphere, the potential $u(\mathbf{y})$ on Γ is computed by the WOS method with 10^5 Brownian paths for each grid of a 40×40 grids generated by evenly discretizing the surface of the hemisphere along with the polar and azimuthal angles. A bilinear interpolation is applied for potentials $u(\mathbf{y})$ on Γ in the numerical quadratures. In the WOS method, a large sphere with radius $R=10^5$ is introduced, and whenever particles move out of this large sphere, they are considered as gone to the infinity [25] and no contribution will be made to the expectation value on the domain boundary in the Feynman-Kac formula. The thickness of the absorption shell $\varepsilon=10^{-5}$ is used to determine if particles have hit the boundary or not.

A general patch S is discretized into triangular panels with the help of distmesh [33] and CGAL tools [34]. For the numerical tests here all cases use the proposed IESK version of the BIE-WOS method. In order to improve the accuracy, a linear BEM is applied for the panels inside a patch, while a constant BEM is applied for the outer-most panels on the patch. The collocation points are exactly located on the corner if the same linear BEM method is applied there (p. 417, [17]). A Gauss quadrature with 40×40 Gauss points is applied for each integration panel. In order to improve the accuracy of quadratures even more, for curve surface, quadratures on curve triangular panel are applied, instead.

The analytical solutions of all three cases are obtained, for the Dirichlet boundary conditions are carefully set as the potentials induced by the charges.

Case 1: Interface between two half-spaces. A $[-15,15]\times[-15,15]$ rectangular plate is located on xoy interface between two dissimilar dielectric half spaces, covered by $16\times$

Table 2: Accuracy and scalability of charge density on the planar interface between two dielectric half-spaces.

Task load	#nodes	#CPU cores	Wall time(s)	Speedup	Max error(%)
1x	1	16	89.06	1.0	1.97
32x	32	512	91.93	32.0	1.97
64x	64	1024	91.65	64.2	1.97
128x	128	2048	106.20	110.8	1.97
256x	256	4096	106.47	221.0	2.43

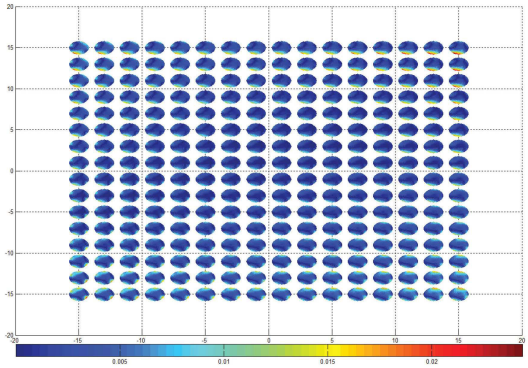

Figure 4: Relative error distribution on the planar interface between two dielectric half-spaces.

16 hemispheres with a radius $a=2$. A unit charge is located at (0,0,-20). The maximal number of computational nodes is 256.

The speedup and maximal relative error are listed in Table 2, where the maximal relative error is 2.43%. A more clear colormap of the relative error distribution on the whole solved surface is shown in Fig. 4, where the relative errors of most regions are less than 1%. The scalability of the parallel BIE-WOS method is shown in Fig. 5. It can be seen that when the number of CPU cores increases from 16 and 4096, the parallel BIE-WOS can nearly keep up the ideal linear speedup.

Case 2: A very large ellipsoid. A very large ellipsoid with semi-axes $e_1=20$, $e_2=30$ and $e_3=40$. Three unit point charges are located at $(0,0,0)$, $(10,0,0)$ and $(0,0,8)$. 242 hemispheres with radius $a=8$ cover the ellipsoid.

The speedup and maximal relative error are listed in Table 3, where the maximal relative error is 3.06%. The colormap of the relative error distribution is shown in Fig. 6, where the relative errors of most regions are smaller than 1%.

The scalability of the BIE-WOS method is shown in Fig. 7, where BIE-WOS algorithm again keeps the nearly ideal linear speedup, when the CPU core number increases from 16 to 3872.

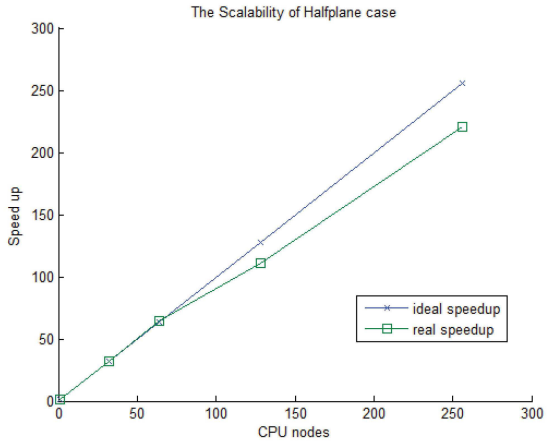

Figure 5: Scalability of the BIE-WOS method on the planar interface between two dielectric half-spaces.

Table 3: Accuracy and scalability of charge density on a large ellipsoid.

Task load	#nodes	#CPU cores	Wall time(s)	Speedup	Max error(%)
1x	1	16	1069.94	1.0	2.35
32x	32	512	1248.94	27.5	2.35
64x	64	1024	1239.91	55.4	2.35
128x	128	2048	1426.46	96.2	2.35
242x	242	3872	1164.05	223.0	3.06

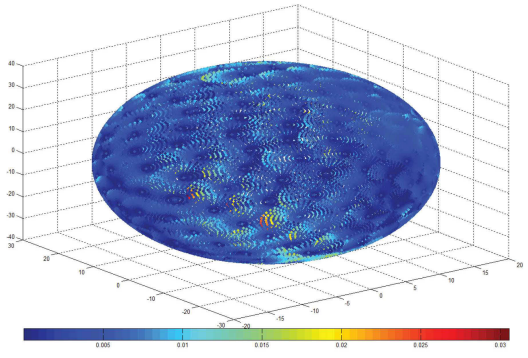

Figure 6: Relative error distribution on a large ellipsoid test case.

Case 3: A body of revolution. A body of revolution is formed by rotating the function $f(x)=(x/2)(x/2-3)(x/2-1.50-0.8i)(x/2-1.5+0.8i), x\in[0,6]$ along x-axis as shown in Fig. 8, and Fig. 9 shows its CAD representation.

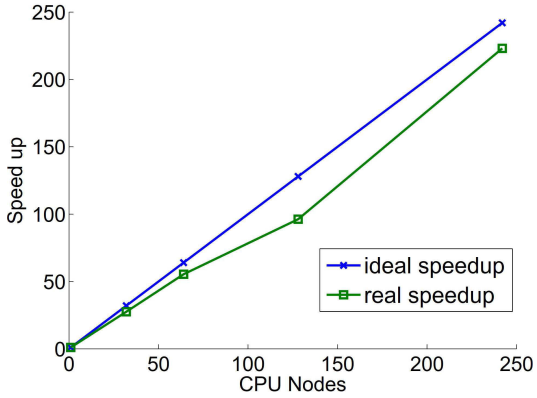

Figure 7: Scalability of the BIE-WOS method on a large ellipsoid.

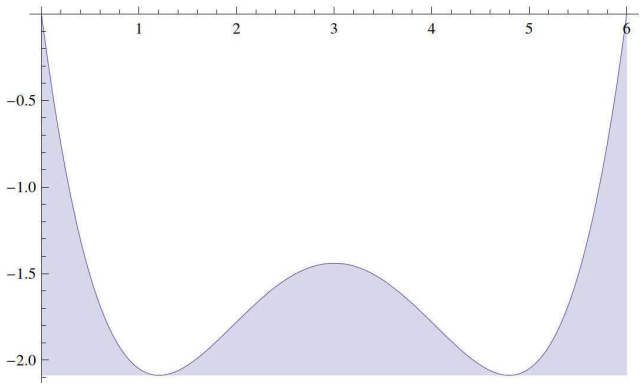

Figure 8: A convolution rotating $f(x)$ along x-axis.

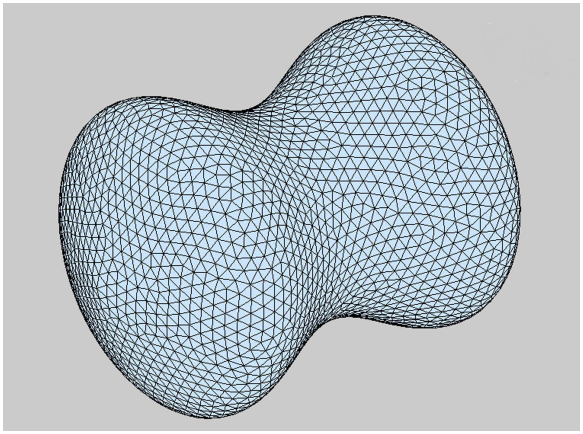

Figure 9: Discretization of a large revolution body.

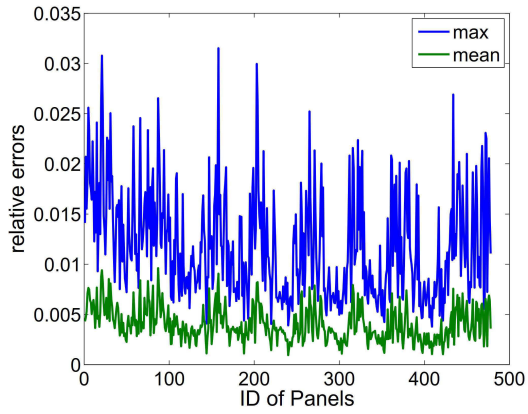

Figure 10: Maximal and mean of relative error over panels.

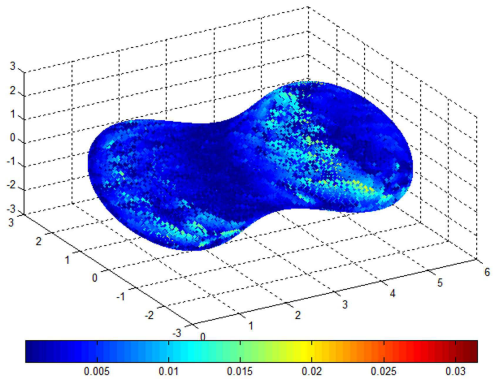

Figure 11: Relative error distribution on a large revolution body.

Table 4: Accuracy and scalability of charge density on a large revolution body.

Task load	#nodes	#CPU cores	Wall time(s)	Speedup	Max error(%)
4x	4	64	1170	4.0	2.07
32x	32	512	1200	31.2	3.08
128x	128	2048	1523	98.3	3.08
180x	180	2880	1480	142.3	3.15
256x	256	4096	1387	215.9	3.15
400x	400	6400	1259	371.7	3.15

The maximal and mean relative error of each hemisphere are shown in Fig. 10, where x-axis is the *id* of hemispheres. From Fig. 10, the maximal relative error of all panels is 3.15% and the maximal of mean relative errors of hemispheres is less than 1%. The

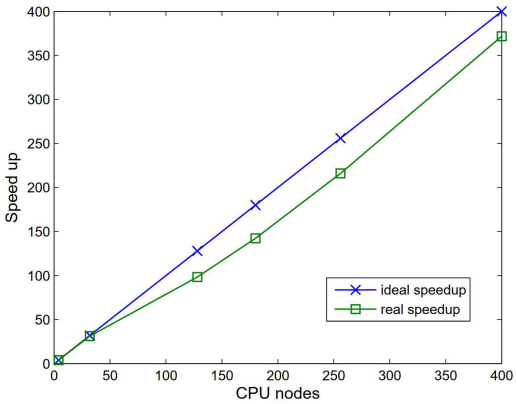

Figure 12: Scalability of a large revolution body.

color-map of the relative error distribution is shown in Fig. 11.

Fig. 12 shows the scalability, which again keeps the nearly ideal linear speedup as the number of CPU cores increases from 64 to 6400.

6 Conclusions and discussions

In this paper, a parallel BIE-WOS solver, without the need of a global structured mesh over the domain boundary, is implemented for the Laplace equation with Dirichlet data with high scalability on large scale computational platforms. The numerical cancelation of the BIE-WOS with the first kind integral equation is analyzed and the BIE-WOS method with the second kind integral is proposed to avoid possible error amplifications in the BIE. For flat patches, the BIE-WOS with IESK can be simplified to obtain all Neumann data, thus more efficient than the original BIE-WOS method. The numerical results verify the accuracy and the desired nearly linear scalability of the algorithm on a supercomputer with 6400 CPU cores. Based on its high scalability, the proposed method can be applied to solve large scale Laplace problems within a constant time by increasing the number of CPU nodes.

An important feature of the parallel BIE-WOS method is its fault tolerance capability for exascale computations, due to the local feature of the boundary domain decomposition approach and the use of path integral ensemble of the WOS methods. Any possible error in computing the DtN mapping on any individual patch of small size over the boundary, due to either computer memory or communication fault, will have only a minimal effect on the overall calculation of the mapping, thus on the solution to the Laplace equation. A simple monitor of the value of the local DtN mapping, compared with the average values from neighboring patches, can be implemented to flag possible fault for re-calculation over the patch of concern.

Finally, though the BIE-WOS method presented in this paper is for the Laplace equation, for the Poisson equation (2.1) with a non-zero right hand side $f(x)$ with a compact support, a special solution $u^*(\mathbf{x})$ in a box enclosing the $\sup(f)$ can be found by inverting the Laplace operator using Fast Fourier Transforms, then a simple subtraction with $u^*(\mathbf{x})$ will reduce the Poisson equation to a Laplace equation with a modified boundary data on $\partial\Omega$, to which the proposed BIE-WOS method can be applied.

Acknowledgments

This work was supported in part by the National Key Research and Development Program of China under Grant 2016YFB0201304, in part by National Natural Science Foundation of China (NSFC) research projects 61674042, 61774045, 61974032, 61929102. W. Cai is supported by US National Science Foundation (Grant No. DMS-1950471).

References

[1] C. Yan, W. Cai, and X. Zeng, A parallel method for solving Laplace equations with Dirichlet data using local boundary integral equations and random walks, SIAM Journal on Scientific Computing, 35 (2013), B868-B889.
[2] W. Yu and Z. Wang, Enhanced QMM-BEM solver for three-dimensional multiple-dielectric capacitance extraction within the finite domain, IEEE Trans. Microw. Theory Techn., 52 (2004), 560-566.
[3] K. Nabors and J. White, Fastcap: A multipole accelerated 3-D capacitance extraction program, IEEE Trans. Comput.-Aided Design Integr. Circuits Syst., 10 (1991), 1447-1459.
[4] J. R. Phillips and J. White, A precorrected-FFT method for capacitance extraction oy f complicated 3-D structures, in Proceedings of the 1994 IEEE/ACM international conference on Computer-Aided Design, IEEE Computer Society Press, 1994, 268-271.
[5] W. Shi, J. Liu, N. Kakani, and T. Yu, A fast hierarchical algorithm for three-dimensional capacitance extraction, IEEE Trans. Comput.-Aided Design Integr. Circuits Syst., 21 (2002), 330-336.
[6] S. Yan, V. Sarin, and W. Shi, Sparse transformations and preconditioners for 3-D capacitance extraction, IEEE Trans. Comput.-Aided Design Integr. Circuits Syst., 24 (2005), 1420-1426.
[7] G. Chen, H. Zhu, T. Cui, Z. Chen, X. Zeng, and W. Cai, ParAFEMCap: A parallel adaptive finite-element method for 3-D VLSI interconnect capacitance extraction, IEEE Trans. Microw. Theory Techn., 60 (2012), 218-231.
[8] T. Cui, J. Chen, H. Zhu, and X. Zeng, Algorithms in ParAFEMImp: A parallel and wideband impedance extraction program for complicated 3-d geometries, in Proceedings of IEEE International Conference on High Performance and Smart Computing (HPSC), 2016.
[9] Y.C. Hsiao and L. Daniel, Caplet: A highly parallelized field solver for capacitance extraction using instantiable basis functions, IEEE Transactions on Computer-Aided Design of Integrated Circuits and Systems, 35(2015), 458-470.
[10] J. A. Given, C. O. Hwang, and M. Mascagni, First-and last-passage Monte Carlo algorithms for the charge density distribution on a conducting surface, Phys. Rev. E, 66 (2002), 056704-1–8.

[11] K. K. Sabelfeld, Monte Carlo Methods in Boundary Value Problems, Springer Series in Computational Physics, Springer, Berlin, 1991.
[12] C. O. Hwang and J. A. Given, Last-passage Monte Carlo algorithm for mutual capacitance, Phys. Rev. E, 74 (2006), 027701-1–3.
[13] QuickCap NX: High-Accuracy 3D Parasitic Field Solver, https://www.synopsys.com/implementation-and-signoff/signoff/quickcap-nx.html
[14] Y. L. Le Coz and R. B. Iverson, A stochastic algorithm for high speed capacitance extraction in integrated circuits, Solid-State Electron., 35 (1992), 1005-1012.
[15] Y. L. Le Coz, H. J. Greub, and R. B. Iverson, Performance of random-walk capacitance extractors for IC interconnects: A numerical study, Solid-State Electron., 42 (1998), 581-588.
[16] C. A. Brebbia, The Boundary Element Method in Engineering, Pentech Press, London, 1978.
[17] K. E. Atkinson, The Numerical Solution of Integral Equations of the Second Kind, Cambridge University Press, 2009.
[18] J. A. Given and C. O. Hwang, Edge distribution method for solving elliptic boundary value problems with boundary singularities, Phys. Rev. E, 68 (2003), 046128-1–6.
[19] M. I. Freidlin, Functional Integration and Partial Differential Equations, Princeton University Press, Princeton, 1985.
[20] A. Friedman, Stochastic Differential Equations and Applications, Dover Publications, NY, 2006.
[21] K. L. Chung, Green, Brown and Probability, World Scientific, Singapore, 1995.
[22] M. Mascagni and C. O. Hwang, ϵ-shell error analysis for "walk on spheres" algorithms, Math. Comput. Simulation, 63 (2003), 93–104.
[23] M. E. Muller, Some continuous Monte Carlo methods for the Dirichlet problem, Ann. Math. Statist., 27 (1956), 569–589.
[24] M. Mascagni and N. A. Simonov, The random walk on the boundary method for calculating capacitance, J. Comput. Phys., 195 (2004), 465–473.
[25] K. K. Sabelfeld, I. A. Shalimova, and A. Lavrentjeva, Random walk on spheres process for exterior Dirichlet problem, Monte Carlo Methods Appl., 1 (1995), 325–331.
[26] W. Cai, Computational Methods for Electromagnetic Phenomena: Electrostatics in Solvation, Scattering, and Electron Transport, Cambridge University Press, London, 2013.
[27] X. Claeys, R. Hiptmair, and E. Spindler, Second-kind boundary integral equations for scattering at composite partly impenetrable objects, Communications in Computational Physics, 23 (2018), 264-295.
[28] M. Guiggiani and A. Gigante, A general algorithm for multidimensional Cauchy principal value integrals in the boundary element method, J. Appl. Mech., 57 (1990), 906-915.
[29] M. Guiggiani, G. Krishnasamy, T. J. Rudolphi, and F. J. Rizzo, A general algorithm for the numerical solution of hypersingular boundary integral equations, ASME. J. Appl. Mech., 59 (1992), 604-614.
[30] J. Zhu and Z. Yuan, Boundary Element Analysis, Science Press, Beijing, 2009.
[31] The OpenMP API specification for parallel programming, https://www.openmp.org/
[32] Open MPI: Open Source High Performance Computing, https://www.open-mpi.org/
[33] P.-O. Persson and G. Strang, A simple mesh generator in MATLAB, SIAM Review, 46 (2004), 329-345.
[34] CGAL: The Computational Geometry Algorithms Library, https://www.cgal.org/